aerospace

MDPI

Article

# Experimental and Numerical Study on Residual Strength of Honeycomb Sandwich Composite Structure after Lightning Strike

**Yongwei Wang, Deng Zhou, Gang Yan * and Zhuangjie Wang**

State Key Laboratory of Mechanics and Control of Mechanical Structures, College of Aerospace Engineering, Nanjing University of Aeronautics and Astronautics, Nanjing 210016, China; wangyongwei@nuaa.edu.cn (Y.W.); zhoudeng@nuaa.edu.cn (D.Z.); zhuangjie123@nuaa.edu.cn (Z.W.)
* Correspondence: yangang@nuaa.edu.cn

**Abstract:** Honeycomb sandwich composite structures are widely used in various aircraft structures due to their unique performance. However, honeycomb sandwich composite structures are prone to lightning damage that threatens the structure safety. Therefore, it is necessary to assess the residual mechanical properties of honeycomb sandwich composite structures after a lightning strike. In this study, simulated lightning strike tests were first conducted for honeycomb sandwich panels with and without carbon nanotube film (CNTF) to obtain different damage scenarios and study the protection effect of CNTF. Then, the residual compressive strength of the panels with lightning strike damage was predicted using a progressive damage analysis method and verified with the experimental results. It was found that the numerical prediction results agree with the experimental results. The size and extent of lightning damage have an important effect on the compression damage mode of honeycomb sandwich panel with closed edges.

**Keywords:** honeycomb sandwich composite structures; simulated lightning strike tests; residual compressive strength; progressive damage analysis; compression damage mode

check for updates

**Citation:** Wang, Y.; Zhou, D.; Yan, G.; Wang, Z. Experimental and Numerical Study on Residual Strength of Honeycomb Sandwich Composite Structure after Lightning Strike. *Aerospace* **2022**, *9*, 158. https://doi.org/10.3390/aerospace9030158

Academic Editor: Stelios K. Georgantzinos

Received: 28 January 2022
Accepted: 11 March 2022
Published: 14 March 2022

**Publisher's Note:** MDPI stays neutral with regard to jurisdictional claims in published maps and institutional affiliations.

**Copyright:** © 2022 by the authors. Licensee MDPI, Basel, Switzerland. This article is an open access article distributed under the terms and conditions of the Creative Commons Attribution (CC BY) license (https://creativecommons.org/licenses/by/4.0/).

## 1. Introduction

Aircraft are prone to lightning strikes when flying. According to relevant flight statistics, the frequency of a commercial aircraft struck by lightning is about every 1000 to 10,000 h of flight [1]. In the past, the metallic fuselage and wing structures could quickly dissipate the lightning current and protect the aircraft from lightning damage. However, composite materials with excellent performance have gradually replaced traditional metallic materials and become one of the basic materials of aerospace structures [2]. For example, in the Boeing 787 Dreamliner, composite materials account for 50% of the total weight of the structure [3]. Compared with metals, composite materials have lower electrical conductivity, and thus are more sensitive to lightning damage. Without proper lightning protection, the resistive heat generated by the Joule effect can severely damage the integrity of the structure, reduce the mechanical strength and threat flight safety [4,5]. Therefore, it is very important to study the lightning protection methods and residual mechanical properties of composite structures after a lightning strike.

Researchers have already performed many studies on lightning strike protection for composite structures [6–10]. For example, Zhang et al. [11] embedded lightning protection film prepared by mixing CNT and polyether ketone into the interlayer of composite materials and combined a simulated lightning test and numerical simulation to study its protection effect. Liu et al. [12] conducted a numerical study on the direct effect of a lightning strike on composite material with a combination of electro-thermal analysis and blowing out pulse (BOI) analysis. By comparing the results of BOI analysis and a lightning strike test, they found that the strain field corresponds with the damage mode of

the lightning strike sample. Ogasawara et al. [13] conducted thermal-electrical coupling analysis of carbon fiber reinforced polymer (CFRP) under simulated lightning current and compared the numerical results with the experimental results. Based on the numerical results and the thermal decomposition behavior of CFRP, the delamination area and damage depth of CFRP were estimated, and the damage area was found to be in good qualitative agreement with the experimental results. To clarify the damage caused by a lightning strike to composite materials, Qi et al. [14] introduced numerical calculation of the resin pyrolysis degree into electrical-thermal numerical analysis and found that this simulation method is very effective through comparative analysis with a simulated lightning strike experiment.

To evaluate the protection effects and the structural integrity, some researchers have not only studied the lightning damage of composite materials, but also studied their residual mechanical properties after a lightning strike [15–19]. For example, Wang et al. [20] conducted a numerical simulation study on lightning damage characteristics of composite laminates through electrical-thermal-structural analysis and element deletion, while predicting the residual tensile strength of the specimen after a lightning strike with proper failure criterion. The results showed that the residual tensile strength decreases with the increase of the peak value of lightning current under static tensile load. Kumar et al. [21] prepared four types of CFRP plates with different thickness conductivities by replacing traditional epoxy resin with conductive resin and applying simulated lightning current to them. The bending tests after the lightning strike showed that the residual bending strength of specimens with a thickness conductivity of 110 S/m can maintain 92% after lightning strike. Zhao et al. [22] prepared a lightweight conductive veil and interwove it with carbon fiber composite material, which increased its thickness conductivity to 27.9 S/m, and the compression strength retention rate reached 79% after a lightning strike. Wang et al. [23] used different progressive damage analysis methods to simulate the compression failure process of composite laminates after a lightning strike. The results showed that the Hashin criterion had the highest accuracy, and the stress concentration occurred mainly in the angle between the fixed end of composite laminates and the lightning damage zone.

Nonetheless, most of the research objects in previous studies were small-size composite laminates, and there were also some shortcomings in the corresponding lightning protection methods, such as the structural weight increase of metallic protection materials [24,25], galvanic corrosion [26,27] and large-scale manufacturing of lightning protection materials [28,29], which have to be considered. In this study, simulated lightning strike tests were first conducted for honeycomb sandwich panels with and without carbon nanotube film (CNTF) to obtain different damage scenarios and study the protection effect of CNTF. Then, the residual compressive strength of the panels with lightning strike damage was predicted using a progressive damage analysis method and verified with the experimental results. The prediction results of the residual strength of specimens after a lightning strike agree with the results of axial compression experiments, verifying the accuracy of the finite element prediction method.

## 2. Simulated Lightning Strike Test

### *2.1. Materials and Specimens*

Compared with traditional composite laminates, honeycomb sandwich composite structures have good impact resistance and weight reduction characteristics and have been widely used in various aircraft structures [30]. For example, in the Airbus A380, the belly fairing, the nacelles, the front landing gear doors, some ailerons and the rudder are all made with sandwich structures [31]. The honeycomb sandwich panel in this study was mainly composed of carbon fiber preimpregnated cloth with about a 40% resin volume fraction (T300, Jiangsu Tian Niao High-tech Co., Ltd., Wuxi, China), Nomex paper honeycomb (JY1-3.2-48, Jiangsu Jun Yuan New Materials Co., Ltd., Nantong, China) and epoxy resin adhesive film (TS-JM-200, Shandong Wei Hai Guang Wei Composites Co., Ltd., Weihai, China), as shown in Figure 1.

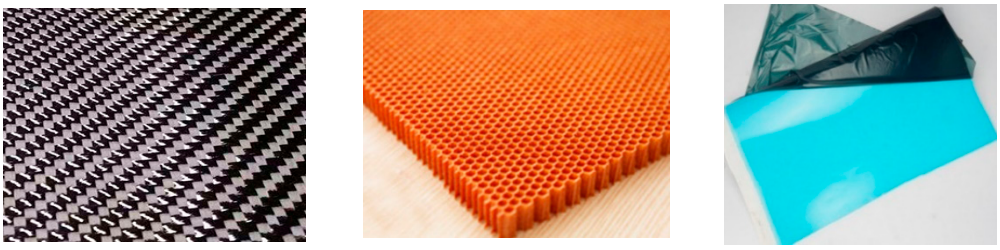

(**a**) (**b**) (**c**)

**Figure 1.** Main materials of honeycomb sandwich panel: (**a**) carbon fiber preimpregnated cloth; (**b**) nomex paper honeycomb; (**c**) epoxy resin adhesive film.

In this study, CNTF (JCNTF-20C, Jicang Nanotechnology Co., Ltd., Nanjing, China) was fabricated by the floating catalytic chemical vapor deposition (FCCVD) method. FCCVD is a relatively simple and low-cost method to produce CNTF. The hydrocarbon source, iron source and sulfur source were continuously injected by flowing hydrogen-carrying gas into the reaction furnace above 1000 °C. Then, CNTs started to grow and entangle together due to Van der Waals forces to form an aerogel sock, which was collected in reels and then densified into CNTF. The as-received CNTF and its related material properties characterized by scanning electron microscopy (SEM) and Raman spectroscopy (RS) are shown in Figure 2. As can be seen from Figure 2a, the surface of the CNTF was relatively uniform and smooth, its thickness was about 12μm and its conductivity was about $1.1 \times 10^5$ S/m. Figure 2b shows the random staggered entanglement of CNTs in CNTF and its high porosity, which can help infiltration of resin improve the binding between the film and the panel. Raman spectra of CNTF in Figure 2c showed that the value of $I_D/I_G$ was small, and the G peak was sharper and denser than the D peak, indicating that the graphitization degree of CNT was good.

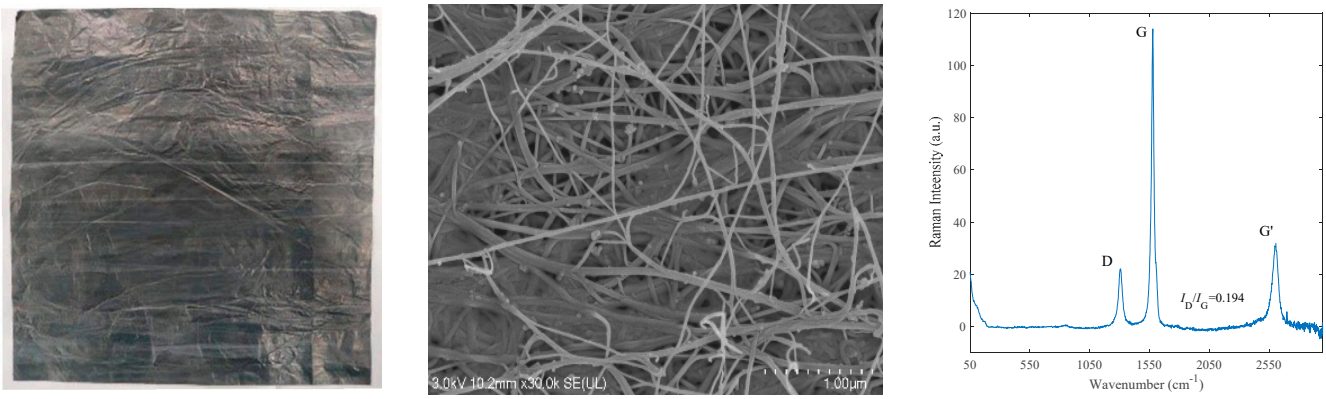


(**a**) (**b**) (**c**)

**Figure 2.** CNTF fabricated by FCCVD and its related properties: (**a**) CNTF samples; (**b**) SEM result; (**c**) RS result.

Two specimens of honeycomb sandwich composite panels were used in this study. One was the unprotected specimen (designated as NS80), and the other was the protected specimen (designated as PS80) containing CNTF on the surface. The fabrication process of the two specimens was consistent, and the configurations and dimensions of the two specimens are shown in Figure 3.

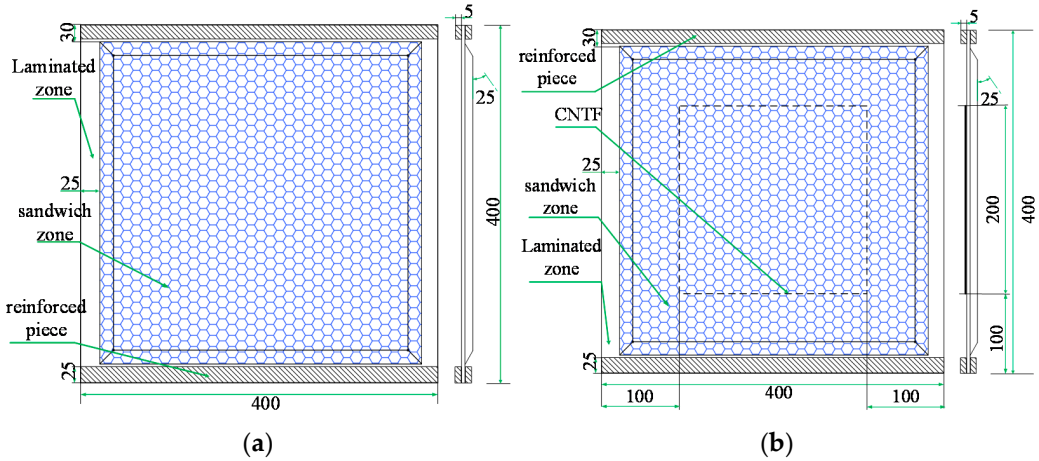


**Figure 3.** Specimen configurations and dimensions: (**a**) unprotected specimen; (**b**) protected specimen.

To approximate a real engineering situation, the edge zone of the sandwich panel was set with a bevel cutting treatment, and the upper and lower skins were closed at the edges, as shown in Figure 3. The thickness of the honeycomb core was 10 mm; the thickness of the single laminated plate at the edges after curing was about 0.21 mm; the laying-up sequence of the laminated zone was [±45/(0,90)/±45/(0,90)/±45/(0,90)/±45/±45/(0,90)/±45/(0,90)/±45], while that of the honeycomb sandwich zone was [±45/(0,90)/±45/(0,90)/±45/$C_{10}$/±45/(0,90)/±45], as shown in Figure 4.

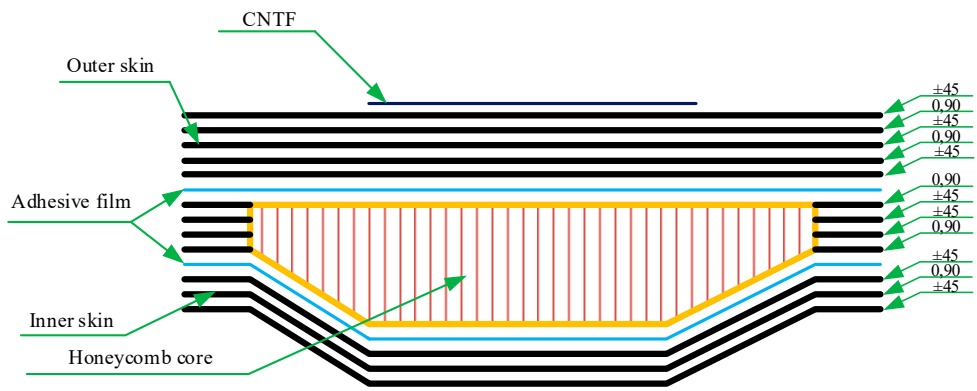


**Figure 4.** Laying sequence of honeycomb panel specimens (not in scale).

When preparing specimens, first, a square CNTF was laid at the center of the carbon fiber preimpregnated cloth (this step can be ignored for unprotected specimens). Then, the carbon fiber preimpregnated cloth, epoxy resin adhesive film and honeycomb core material were laid in a certain sequence and encapsulated together into a vacuum bag. Finally, the specimens were cured and formed under 180 °C and 340 kPa. After curing, the specimens were taken out and machined, and the final specimens are shown in Figure 5.

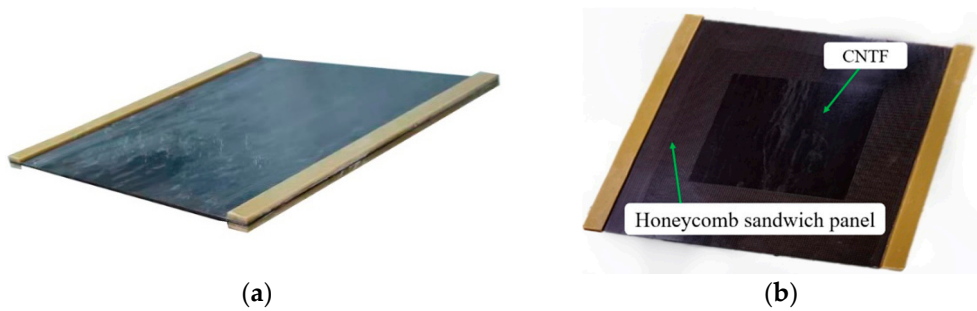


**Figure 5.** Specimens after curing: (**a**) unprotected specimen; (**b**) protected specimen.

### 2.2. Test Setup

To facilitate unified research and analysis of lightning damage, the Society of Automotive Engineers (SAE) organizes the entire change process of the current of an aircraft subjected to a lightning strike into four components: A, B, C and D. Their characteristics are shown in Figure 6a. It can be seen from the figure that the peak value of the A-waveform current component is relatively high, causing more serious damage to the aircraft. Therefore, the double exponential pulse current with peak value of 80 kA and waveform parameters of 8/20 μs was used as the simulation simplification of A-wave lightning current and then applied to two kinds of specimens for the simulated lightning strike test. The definition of waveform parameters of the double exponential pulse current $t_1/t_2$ are shown in Figure 6b, where $t_1$ represents the time for the current to increase from 10% of the peak value to 90%, while $t_2$ represents the time for the current to increase from 10% of the peak value to the maximum value and then decrease to 50% of the peak value.

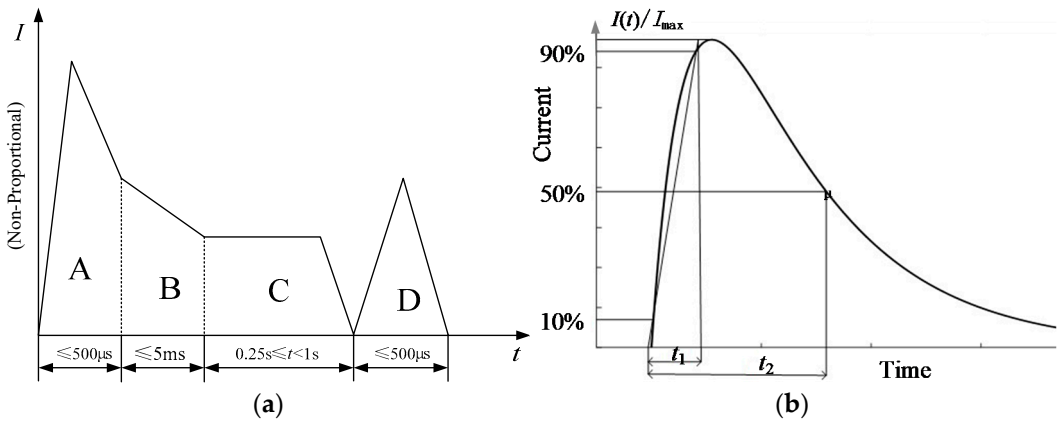


**Figure 6.** Current waveform standard of simulated lightning strike test: (**a**) standard current waveform Data from [32]; (**b**) double exponential pulse waveform.

In this study, the high intensity lightning current applied to the specimen was generated by the pulse current generator and finally released by the conductive copper probe above the specimen. Due to the large impulse of the excitation current, the left and right sides of the honeycomb specimen were pressed and fastened with bayonet pliers to the fixture to avoid the honeycomb sandwich panel being knocked off during the test, thus affecting the test effect. At the same time, to ensure the safety of the simulated lightning strike test, grounded copper wire was used to connect with the copper fixture fixed on both sides of the specimen so that the left and right ends of the specimen were always grounded during the test process. Meanwhile, conductive copper foil was used to connect the CNTF and both ends of the specimen to form a current loop.

To facilitate study of the changes of the applied excitation current during the test, an oscilloscope was used to collect the waveform of the excitation current. The final acquisition results are shown in Figure 7a. Since the process of a simulated lightning strike test is very short, we filmed its discharge process by high-speed camera. The result is shown in Figure 7b. When the excitation current was released, dazzling white light was observed in the current injection zone of the specimen, followed by a huge sound, and then the white light gradually disappeared. Burning flames and sputtering sparks were observed on the surface of the specimen. Finally, the flame gradually decreased or even disappeared, resulting in white smoke.

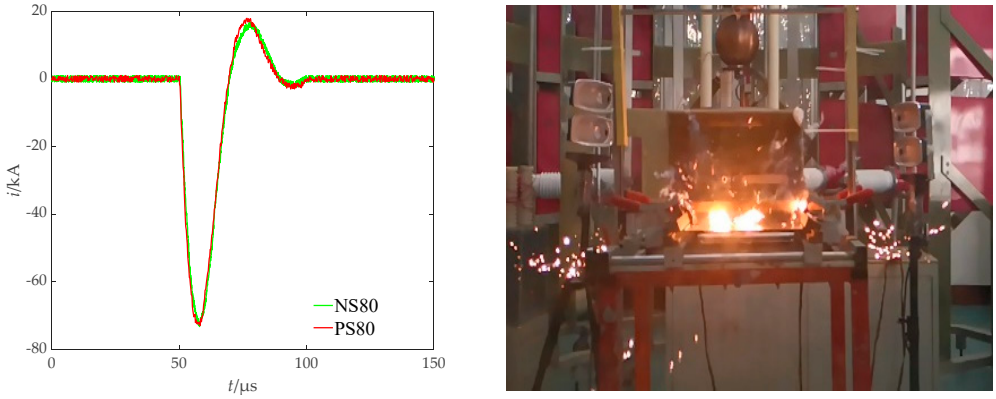


(**a**) (**b**)

**Figure 7.** Acquisition results of simulated lightning strike test: (**a**) test current waveform; (**b**) simulate lightning test phenomenon.

### 2.3. Results and Discussion

The damage of honeycomb sandwich panel caused by lightning mainly includes visible in-plane damage of skin and invisible damage of inner thickness direction. To specifically analyze the lightning damage status, visual inspection was carried out on the surface skin after a lightning strike to determine the approximate in-plane damage range. Then, an image processing software was used to divide the damaged zone and measure the size of the damaged zone. The final results are shown in Figure 8. Finally, X-ray CT scanning technology was used to conduct nondestructive scanning and reconstruct sections of the damage in the direction of internal thickness of the honeycomb sandwich panel specimen, and the relevant damage dimensions were marked. The results are shown in Figure 9.

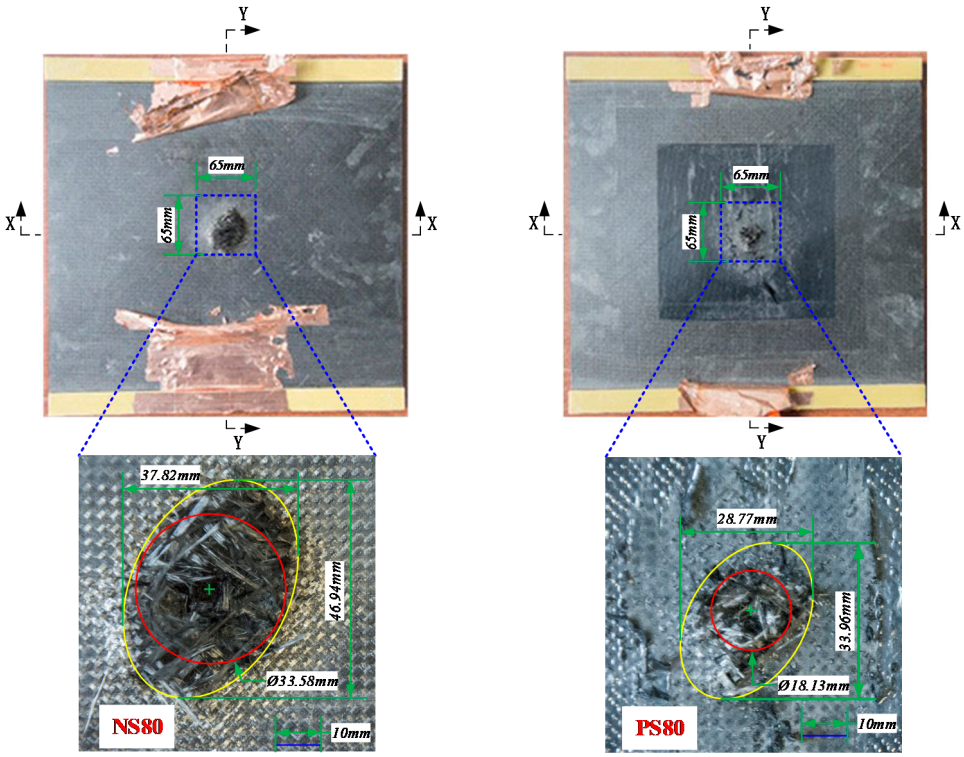


(**a**) (**b**)

**Figure 8.** Apparent damage of specimens: (**a**) NS80 specimen; (**b**) PS80 specimen.

It can be seen from Figure 8, with the lightning strike point as the center, the surface outer skin shows different degrees of lightning strike damage. The damage forms of external skin caused by the lightning strike mainly include ablative evaporation of epoxy resin, fiber warping and fracture. Meanwhile, large area tearing and ablative disappearance of surface CNTF can also be observed for protected specimens. To quantify the degree of lightning damage, we divided the lightning damage in Figure 8 into different zones according to the degree of damage. The outermost ellipse represents "resin damage", while the inner circular zone represents "fiber damage". The area of ellipse was measured as "damage area" for comparative analysis. At the same time, the diameter of the circle was measured to provide data support for the subsequent numerical simulation of residual strength. Similarly, the maximum length of delamination damage on the lightning center point section in Figure 9 was defined as "delamination length" and measured. Finally, the damage in Figures 8 and 9 was sorted out and summarized as shown in Table 1.

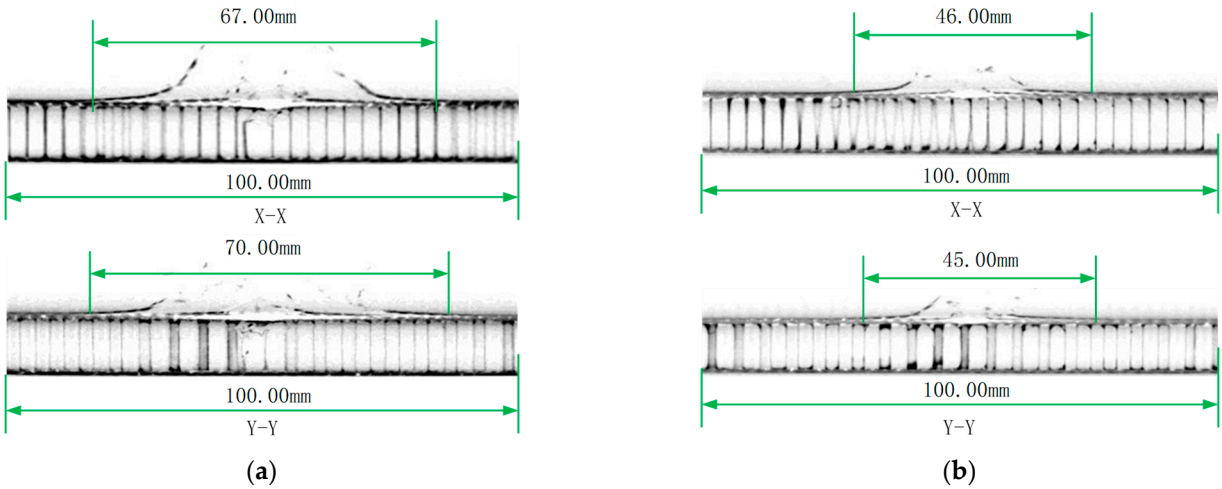


**Figure 9.** Internal damage images by X-ray CT scanning: (**a**) scanning results of the NS80 specimen; (**b**) scanning results of the PS80 specimen.

**Table 1.** Data of lightning damage extent.

| Specimen | Damage Area/mm$^2$ | Delamination Length/mm |
|---|---|---|
| NS80 | 1313 | 70 |
| PS80 | 742 | 46 |
| Damage reduction rate | 43.49% | 34.29% |

It can be clearly seen from the data in the table that when the peak current was 80 kA, the surface "damage area" and internal "delamination length" of the honeycomb sandwich specimen with CNTF on the surface were reduced by 43.49% and 34.29%, respectively, compared with the unprotected specimen. These data demonstrate the lightning protection effect of CNTF on honeycomb sandwich panel.

## 3. Axial Compression Test

### *3.1. Test Setup*

To study the residual mechanical properties of a honeycomb sandwich panel after a lightning strike, axial compression tests were carried out on the two specimens after a lightning strike to measure their residual compression strength. Meanwhile the compression strength results of the undamaged specimen (NS00) in the existing literature were used as a reference.

To study the damage distribution of a honeycomb sandwich panel specimen in the axial compression test process, resistive strain gauges were pasted on the weak zone of the

specimen for damage detection in the compression process. The final strain gauge layout of the honeycomb sandwich specimen is shown in Figure 10.

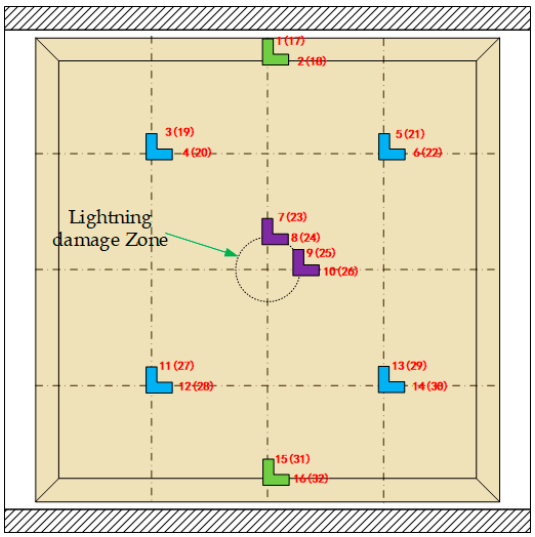


**Figure 10.** Layout of strain gauges.

These strain gauges can be roughly divided into three groups, and the specific strain numbers and locations are shown in Table 2, where odd numbers represent the longitudinal strain gauge number and even numbers represent the transverse strain gauge number. No parentheses represent the strain gauge number on the inner skin side of the specimen, while the values in parentheses represent the strain gauge number at the corresponding position on the outer skin side of the specimen.

**Table 2.** Strain gauge array information.

| | First Group Strain | Second Group Strain | Third Group Strain |
|---|---|---|---|
| Number | 1(17)\2(18)<br>15(31)\16(32) | 3(19)\4(20)\5(21)\6(22)<br>11(27)\12(28)\13(29)\14(30) | 7(23)\8 (24)<br>9 (25)\10 (26) |
| Position | Chamfer | 1/4 honeycomb core | Lightning damage around |

As the size of the specimen was relatively large, a special compression test fixture was manufactured for this purpose. The test status is shown in Figure 11. During the axial compression test, the displacement was loaded by a multifunctional fatigue testing machine (Landmark 370.50, MTS Systems Co., Ltd., U.S.A) at a loading speed of 0.5 mm/min. The strain data of the two specimens during the compression test were collected by a static strain data acquisition system (JM3813, Yangzhou Jingming Technology Co., Ltd., Yangzhou, China).

### *3.2. Results and Discussion*

The load-displacement curves of the unprotected specimen (NS80) and the protected specimen (PS80) are shown in Figure 12. It can be seen from the figure that the curves of the two specimens changed approximately linearly before the specimens failed, and the data in the figure show that the residual compression strength of the protected specimen was much larger than that of the unprotected specimen. The strain changes of different parts of the specimen during compression are shown in Figure 13. From the variation trend of strain in the figure, we can roughly judge the damage initiation, distribution and evolution in the specimen.

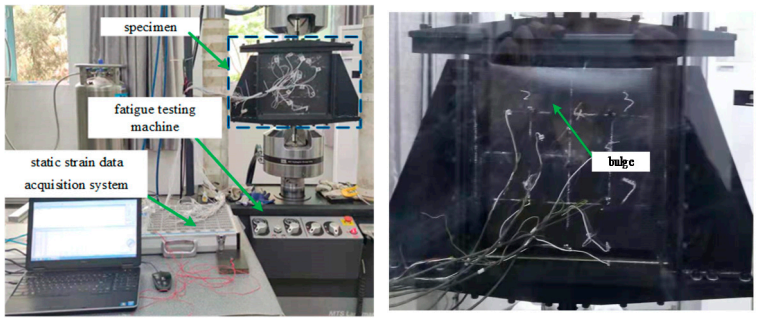


(**a**) (**b**)

**Figure 11.** Axial compression test: (**a**) axial compression test site; (**b**) specimen failure scenario.

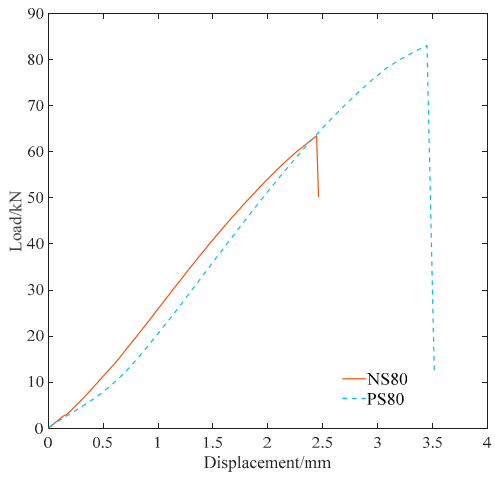


**Figure 12.** Load-displacement curve of the specimens.

For the NS80 specimen, it can be seen from Figure 13 that when the compression load was about 29 kN, the strain gauge (#17) at the chamfering position of the outer skin of the specimen changed, indicating that local compression failure occurred at the chamfering position of the outer skin. When the load was about 44 kN, the strain gauges (#3, #5, #11, #13) at the 1/4 honeycomb position of the inner skin and the strain gauges (#7, #9) around the lightning damage center of the inner skin all changed, indicating that the yield failure occurred at the 1/4 honeycomb position and around the lightning damage of the NS80 specimen. As the load continued, when the load value reached 56 kN, the strain gauge (#31) at the chamfering position changed, indicating that the chamfering position at the lower part of the outer skin of the specimen was damaged at this time.

For the PS80 specimen with CNTF surface protection, it also can be seen from Figure 13 that when the compression load was about 58 kN, the strain gauge at the inner skin oblique position (#1, #15), the strain gauge of inner skin (#3, #5, #11, #13) and the strain gauge around the lightning strike damage center of inner skin (#7, #9) began to change at the same time, indicating that the overall yield instability of the specimen inner skin occurred at this time.

By comparing the load changes of the two specimens, it can be found that compared with the unprotected specimen, the critical buckling load of the inner skin of the surface CNTF protected specimen increased from 48 kN to 58 kN, and its bearing improved to some extent.

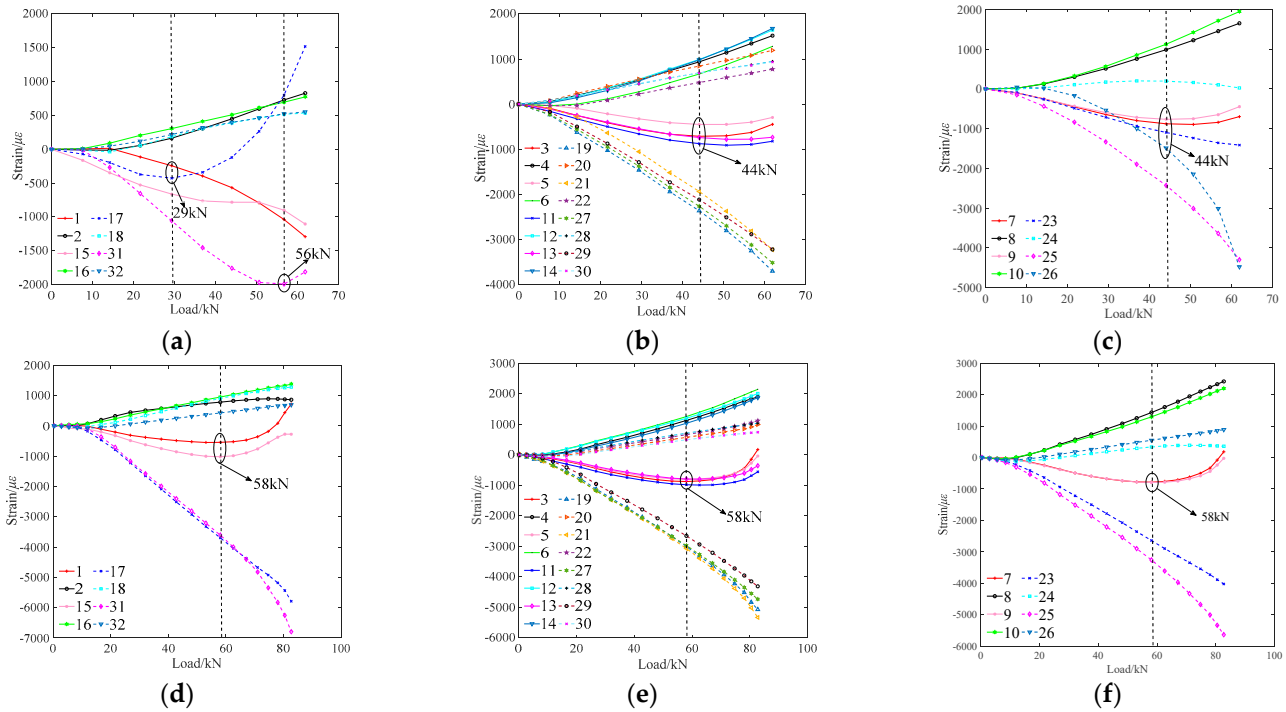


**Figure 13.** Strain collection results of specimens: (**a**) the first group strain results of the NS80 specimen; (**b**) the second group strain results of the NS80 specimen; (**c**) the third group strain results of the NS80 specimen; (**d**) the first group strain results of the PS80 specimen; (**e**) the second group strain results of the PS80 specimen; (**f**) the third group strain results of the PS80 specimen.

The failure modes of the two types of specimens are shown in Figure 14. It can be seen from the figure that the compression failure of the honeycomb sandwich panel specimens with lightning damage mainly occurred in the outer skin, the failure of the unprotected specimen mainly occurred in the center of the panel, while the failure of the protected specimen mainly occurred in the chamfer zone of the skin. The main reason is that the lightning damage at the center of the NS80 specimen is much larger than that of PS80. Under the application of the axial compression load, the compression failure of the NS80 specimen first occurred at the lightning damage in the center, while the failure of the PS80 specimen first occurred at the weak chamfering zone of the structure.

Finally, the peak loads of the two specimens were compared with the averaged compression strength value of three undamaged specimens in the literature [33]. The undamaged specimens were manufactured with the same materials and fabrication methods as the two specimens used in this study. As shown in Table 3, the compression strength of the protected specimen was close to that of the undamaged specimen. The residual compressive strength of the honeycomb sandwich panel specimen protected by the CNTF was about 20% higher than that of the unprotected specimen, which also indicates that the surface CNTF can effectively suppress lightning damage and then improve the residual mechanical properties of the specimens after a lightning strike.

**Table 3.** Residual compression strength data.

| Specimen | NS00 | NS80 | PS80 |
|---|---|---|---|
| Peak load/kN | 96.05 | 63.44 | 83.04 |
| Residual strength | 100% | 66.05% | 86.45% |

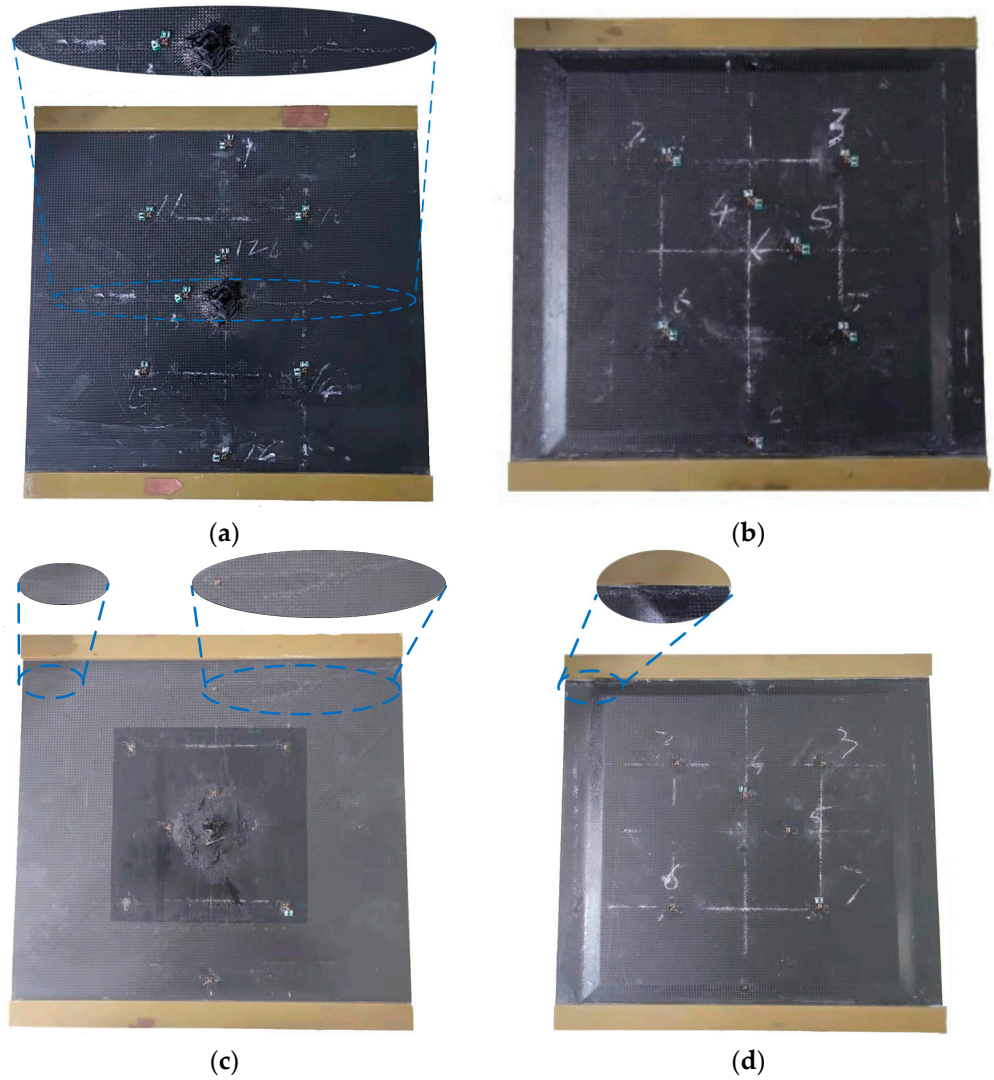

**Figure 14.** Axial compression damage morphology: (**a**) the outer skin side of the NS80 specimen; (**b**) the inner skin side of the NS80 specimen; (**c**) the outer skin side of the PS80 specimen; (**d**) the inner skin side of the PS80 specimen.

## 4. Numerical Simulation

### *4.1. Failure Criteria and Material Degradation*

#### 4.1.1. Mechanical Properties of Materials

The honeycomb sandwich panel specimen was mainly composed of skin, honeycomb core and adhesive film. Failure criteria and material degradation modes of these three parts should be considered respectively during numerical simulation of the specimen. Their mechanical property parameters are shown in Tables 4–6, respectively.

**Table 4.** Mechanical properties of skin Data from [33].

| $E_1$/GPa | $E_2$/GPa | $G_{12}$/GPa | $G_{13} = G_{23}$/GPa | $\nu_{12}$ |
|---|---|---|---|---|
| 58 | 58 | 5 | 2.5 | 0.044 |
| $X_T$/MPa | $X_C$/MPa | $Y_T$/MPa | $Y_C$/MPa | $S_{12}$/MPa |
| 549 | 384 | 504 | 362 | 85 |

**Table 5.** Equivalent mechanical properties of honeycomb cores Data from [33].

| $E_1$/MPa | $E_2$/MPa | $E_3$/MPa | $G_{12}$/MPa | $G_{13}$/MPa | $G_{23}$/MPa | $\nu_{12}$ | $\nu_{13} = \nu_{23}$ |
|---|---|---|---|---|---|---|---|
| 0.1953 | 0.1953 | 136 | 0.073 | 40 | 23 | 0.94 | 0.0003 |
| | $X_{TT}$/MPa | | | $S_{LT}$/MPa | | | $S_{WT}$/MPa |
| | 1.93 | | | 1.26 | | | 0.62 |

**Table 6.** Mechanical properties of adhesive film Data from [33].

| $E$/GPa | $G$/GPa | $\nu$ | $t_n$/MPa | $t_s = t_t$/MPa | $G_n$/N·mm$^{-1}$ | $G_s = G_t$/N·mm$^{-1}$ |
|---|---|---|---|---|---|---|
| 3.2 | 1.23 | 0.3 | 58 | 65 | 0.744 | 3.816 |

4.1.2. Skin Damage

In this study, the skin in the honeycomb sandwich panel was relatively thin, which can be regarded as the plane stress state, so the two-dimensional Hashin criterion [34,35] was adopted to determine whether the skin failed and the type of failure mode. Meanwhile, a stiffness degradation model based on continuous damage mechanics was adopted to characterize the stiffness degradation of skin.

The specific expressions of the two-dimensional Hashin criterion are as follows:

Fiber tensile failure:

$$F_{ft} = \left(\frac{\sigma_{11}}{X_T}\right)^2 + \alpha\left(\frac{\sigma_{12}}{S_L}\right)^2 = 1 \quad (\sigma_{11} \geq 0) \tag{1}$$

Fiber compression failure:

$$F_{fc} = \left(\frac{\sigma_{11}}{X_C}\right)^2 = 1 \quad (\sigma_{11} \leq 0) \tag{2}$$

Matrix tensile failure:

$$F_{mt} = \left(\frac{\sigma_{22}}{Y_T}\right)^2 + \left(\frac{\sigma_{12}}{S_L}\right)^2 = 1 \quad (\sigma_{22} \geq 0) \tag{3}$$

Matrix compression failure:

$$F_{mc} = \left(\frac{\sigma_{22}}{2S_T}\right)^2 + \left[\left(\frac{Y_C}{2S_T}\right)^2 - 1\right]\frac{\sigma_{22}}{Y_C} + \left(\frac{\sigma_{12}}{S_L}\right)^2 = 1 \quad (\sigma_{22} \leq 0) \tag{4}$$

where, $X_T$, $X_C$, $Y_T$, $Y_C$, $S_L$ and $S_T$ are the fiber tensile and compressive strength, matrix tensile and compressive strength and longitudinal and transverse shear strength of the skin material, respectively; $\sigma_{11}$, $\sigma_{22}$ and $\sigma_{12}$ are the effective stress components of the material, $\alpha$ is influence coefficient of shear stress in the fiber tensile damage, between 0 and 1; $F_{ft}$, $F_{fc}$, $F_{mt}$ and $F_{mc}$ represent the damage failure function values of fiber tensile, fiber compression, matrix tensile and matrix compression respectively. When the failure function value reaches 1, it indicates that the corresponding damage occurs.

The specific expressions of stiffness degradation model of skin are shown as follows:

$$\begin{cases} d_m = \begin{cases} d_m^t(\sigma_{22} \geq 0) \\ d_m^c(\sigma_{22} \leq 0) \end{cases} \quad d_f = \begin{cases} d_f^t(\sigma_{11} \geq 0) \\ d_f^c(\sigma_{11} \leq 0) \end{cases} \\ d_s = 1 - \left(1 - d_f^t\right)\left(1 - d_f^c\right)\left(1 - d_m^t\right)\left(1 - d_m^c\right) \end{cases} \tag{5}$$

Among them:

$$d_i^j = \frac{\delta^i(\delta - \delta^0)}{\delta(\delta^i - \delta^0)}, (i = f, m; j = t, c) \tag{6}$$

where, $d_f$, $d_m$ and $d_s$ represent the fiber damage state variable, matrix damage state variable and shear damage state variable of the skin, respectively; their values are between 0 and 1; 0 represents the intact material and 1 represents complete damage; $\delta^0$, $\delta$ and $\delta^i$ represent the initial displacement of damage, the real-time displacement of damage and the final failure displacement, respectively.

#### 4.1.3. Honeycomb Core Damage

In the finite element model, the equivalent model of honeycomb core in the specimen was built based on sandwich plate theory [36,37]. Considering the damage of the honeycomb core during the compression process, the failure and damage evolution of the honeycomb core were determined by writing a user-defined field variable subroutine (USDFLD) based on Besant criterion [38] and direct stiffness degradation theory [39].

The specific form of Besant criterion used to judge honeycomb core failure is as follows:

$$F_{core}^2 = \left(\frac{\sigma_{TT}}{X_{TT}}\right)^n + \left(\frac{\sigma_{LT}}{S_{LT}}\right)^n + \left(\frac{\sigma_{WT}}{S_{WT}}\right)^n \tag{7}$$

where, $\sigma_{TT}$, $\sigma_{LT}$, and $\sigma_{WT}$ represent the normal stress of the honeycomb core in the $T$ direction and the shear stress in the $LT$ and $WT$ directions respectively. $X_{TT}$, $S_{LT}$ and $S_{WT}$ represent the compressive strength and shear strength corresponding to the honeycomb core, respectively. The value of $n$ is 2, when the value of $F_{core}$ reaches 1, the failure of honeycomb core is considered.

The direct stiffness degradation method of honeycomb core is as follows:

$$\left(E'_{11}, E'_{22}, E'_{33}, G'_{12}, G'_{13}, G'_{23}\right)^{\mathrm{T}} = \lambda(E_{11}, E_{22}, E_{33}, G_{12}, G_{13}, G_{23})^{\mathrm{T}} \tag{8}$$

where, $(E'_{11}, E'_{22}, E'_{33}, G'_{12}, G'_{13}, G'_{23})^{\mathrm{T}}$ is the material stiffness after degradation, λ is the corresponding stiffness reduction coefficient, and its value is 0.1 in the numerical calculation model.

#### 4.1.4. Adhesive Film Damage

In this study, the adhesive film was replaced by the cohesive zone model based on the bilinear constitutive model. The quadratic nominal stress criterion [40] was used as the initial damage criterion of the cohesive force model, and the B-K criterion [41] was used to predict the crack propagation based on the damage evolution mode of energy.

The specific expression of the secondary stress criterion used to judge the damage of the cohesive zone model is as follows:

$$\left(\frac{\langle\sigma_n\rangle}{N_{max}}\right)^2 + \left(\frac{\sigma_s}{S_{max}}\right)^2 + \left(\frac{\sigma_t}{T_{max}}\right)^2 = 1 \tag{9}$$

where, < > is the Macaulay bracket; $\sigma_n$, $\sigma_s$ and $\sigma_t$ represent the normal stress of the adhesive film and the nominal stresses in the two shear directions, respectively; while $N_{max}$, $S_{max}$ and $T_{max}$ are the corresponding peak strengths, respectively.

The specific expression of B-K criterion based on energy damage evolution is as follows:

$$G_{IC} + (G_{IIC} - G_{IC})\left\{\frac{G_{II} + G_{III}}{G_I + G_{II} + G_{III}}\right\}^{\eta} = G_C \tag{10}$$

where, $G_I$, $G_{II}$ and $G_{III}$ are the strain energy release rates of normal phase and two tangential directions respectively; $G_{IC}$, $G_{IIC}$ and $G_{IIIC}$ are the fracture toughness of type $I$, type $II$ and type $III$ cracks, respectively; $\eta$ is an interaction parameter; $G_C$ is the critical strain energy

release rate obtained according to B-K criterion; when the value of $G$ reaches $G_C$, the crack begins to expand.

### *4.2. Finite Element Model and Boundary Conditions*

The finite element model of honeycomb sandwich specimen and the setting of relevant boundary conditions are shown in Figure 15. Among them, the arrow $T$ indicates the 0° direction of the skin material. In this finite compression model, continuous shell element SC8R (green element) is used to simulate the skin, three-dimensional solid element C3D8 (brown element) is used to simulate the honeycomb core, and the cohesive element COH3D8 (blue element) is used to simulate the adhesive film. Considering the computational accuracy and efficiency, the global control size of the mesh seeds was set to 5 mm while mesh densities in the chamfer and central zones were further increased. To ensure the continuity of element node displacement, the skin, honeycomb core and adhesive film were connected through the common node, and the strength failure criterion above was used to judge the failure of each part of the specimen in the compression process.

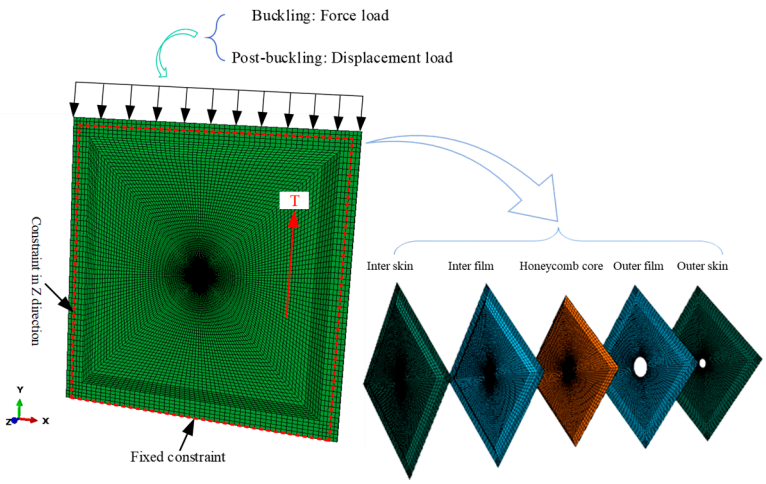


**Figure 15.** Schematic diagram of finite element model and boundary conditions.

As observed in Figures 8 and 9, the outer skins of the honeycomb sandwich specimens were penetrated by the simulated lightning strike. Thus, in the finite element model, the lightning damage of the outer skins and outer films are simplified as circular holes, as shown in Figure 15. The diameters of the holes in outer skins are consistent with the red fiber damage circles in Figure 8, while the diameters of the holes in outer films are consistent with the "delamination length" of the specimens in Figure 9. The size data of the lightning damage for different types of specimens in the models are shown in Table 7.

Taking the clamping state of the specimen in the axial compression test as reference, the boundary conditions of the finite element model are set as shown in Figure 15. The bottom of the specimen is fixed, and constraints in the $z$ direction are set in all four sides. First, based on the buckling module of ABAQUS/Standard solver, the force load was applied to the top of the specimen for structural linear buckling analysis. According to the analysis results, the node information obtained was introduced into the postbuckling analysis model as the initial defect. Then, based on the static general module, the keywords were modified and the force load was replaced by the displacement load for postbuckling analysis.

**Table 7.** Damage dimensions of different specimen models.

| Specimen | NS00 | NS80 | PS80 |
|---|---|---|---|
| Diameter of damage of outer film/mm | 0 | 70 | 46 |
| Diameter of outer skin damage/mm | 0 | 34 | 18 |

### *4.3. Results and Discussion*

#### 4.3.1. Effect of Lightning Damage Degree on Stability

The linear buckling analysis results of different specimens are shown in Figure 16, which mainly includes the first-order buckling mode (FBM) and the second-order buckling mode (SBM) of the specimens. According to the description in relevant literature [42], the compression instability modes of honeycomb sandwich panel were divided into three types, namely, global instability, mixed instability and local instability. It can be clearly seen from the figure that the first two modes of buckling of the NS00 specimen were global stable, while the first two modes of buckling of the PS80 specimen and the NS80 specimen were local instable.

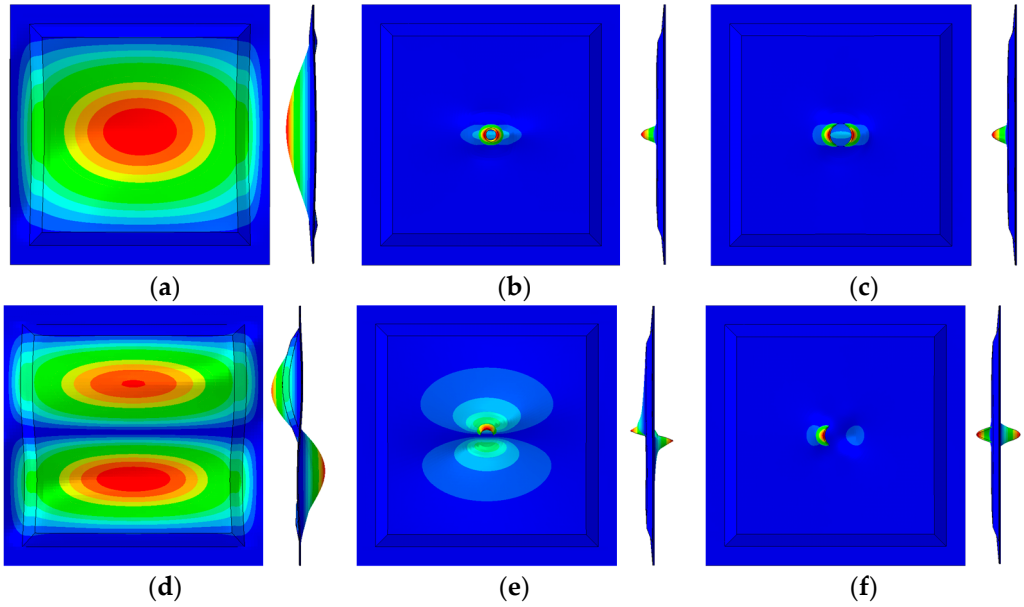


**Figure 16.** Compressive buckling modes of specimens: (**a**) first order buckling mode of the NS00 specimen; (**b**) first order buckling mode of the PS80 specimen; (**c**) first order buckling mode of the NS80 specimen; (**d**) second order buckling mode of the NS00 specimen; (**e**) second order buckling mode of the PS80 specimen; (**f**) second order buckling mode of the NS80 specimen.

#### 4.3.2. Effect of Damage Size and Extent on Residual Strength

To predict the residual compressive strength of the honeycomb sandwich specimen after a lightning strike, it was necessary to introduce the initial geometric defects into the nonlinear postbuckling analysis of the specimen. The node displacement data of FBM was introduced into the nonlinear buckling model as the initial defect for failure analysis, and then the failure loads and failure modes of specimens were obtained by nonlinear buckling analysis. The load displacement curves of the NS00 specimen, the PS80 specimen and the NS80 specimen obtained through numerical simulation are shown in Figure 17. As can be seen from the curves in the figure, the residual compressive strength of the PS80 specimen is not significantly different from that of NS00, while the residual compressive strength of the NS80 specimen decreased significantly.

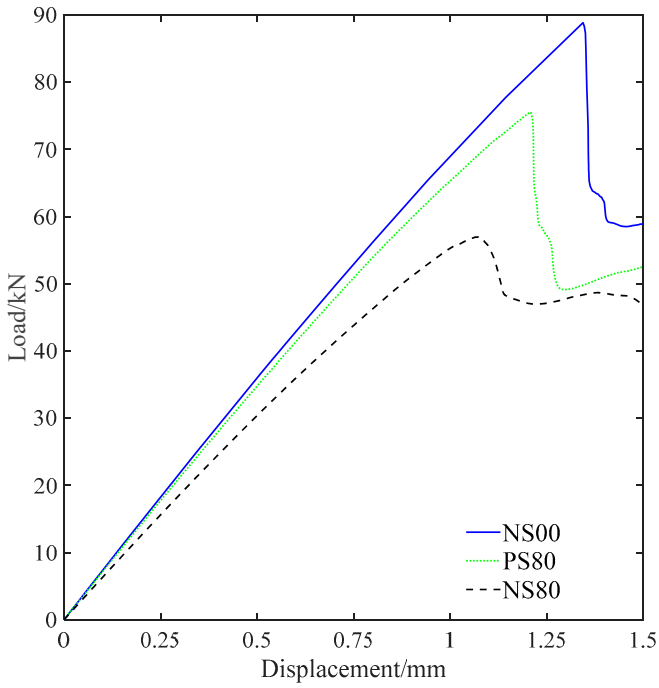


**Figure 17.** Simulated load-displacement curve of specimen.

The failure load calculated by nonlinear buckling analysis was compared with the test value, and the results are shown in Table 8. It can be seen from the data in the table that the relative error between numerical simulation data and test data of all specimens was within 20%. These relative error data indicate that the finite element model can effectively predict the residual strength of honeycomb sandwich panel after a lightning strike to a certain extent.

**Table 8.** Residual strength data of specimens.

| Specimen | NP00 | P80 | NP80 |
|---|---|---|---|
| Test value/kN | 96.05 | 83.04 | 63.44 |
| Prediction value/kN | 88.86 | 75.57 | 56.96 |
| Relative error | −7.49% | −8.90% | −10.21% |

In the compression process, the outer skin was the main load-bearing structure of the honeycomb sandwich panel, and the failure mainly occurred on this side, while the inner skin side usually appeared buckling instability. According to the nonlinear buckling analysis results of the specimen, it was found that there was no obvious damage on the adhesive film, which was relatively consistent with the test results; so only the damage of the honeycomb core and skin was analyzed here.

The skin damage distribution of the NS00, PS80 and NS80 specimens is shown in Figures 18–20, respectively. The red part represents the damaged element, while the blue part represents the undamaged element, respectively. According to the two-dimensional Hashin criterion mentioned above, the skin damage types can be mainly divided into four categories: fiber tensile damage (FTD), fiber compression damage (FCD), matrix tensile damage (MTD) and matrix compression damage (MCD).

It can be seen from Figure 18 that under compression loading, skin damage of the NS00 specimen was mainly distributed in the chamfering zone of the specimen. Skin damage distribution of the PS80 specimen in Figure 19 is similar to that of the NS00 specimen. Skin damage of the NS80 specimen in Figure 20 is mainly distributed around the lightning strike damage in the middle of the skin. The main reason may be that the lightning damage zone

in the middle of the skin of the NS80 specimen is too large, and the stress concentration is significant, which leads to damage before the damage in the chamfer zone occurs.

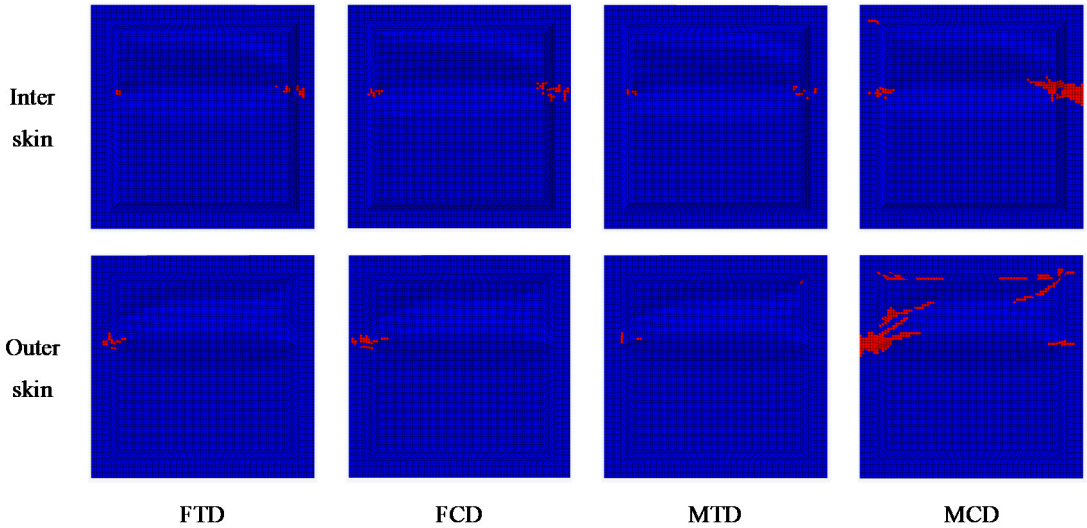


**Figure 18.** Damage distribution of skin in the NS00 specimen.

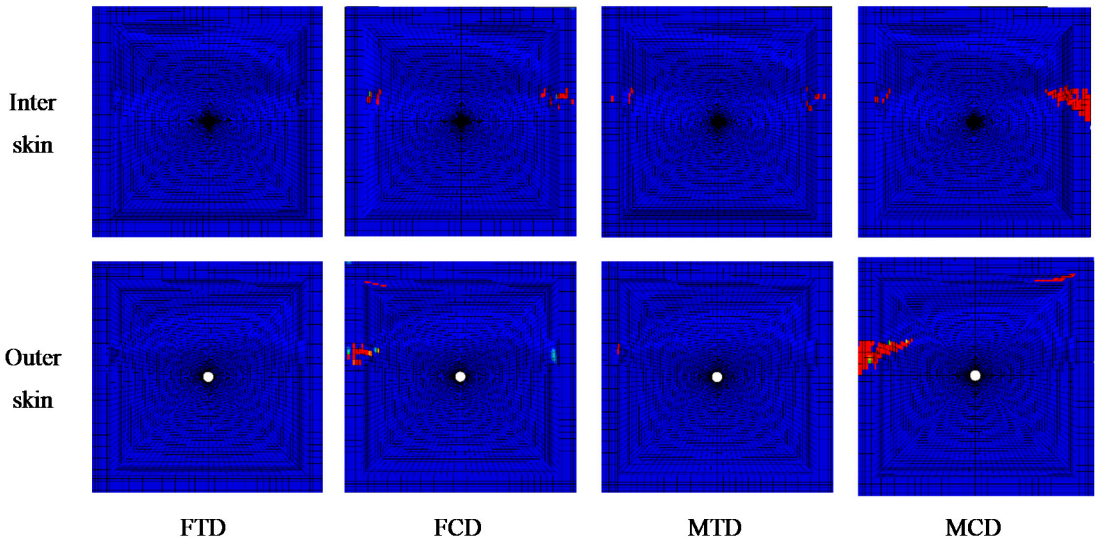


**Figure 19.** Damage distribution of skin in the PS80 specimen.

The damage distribution of the honeycomb core of the NS00, PS80 and NS80 specimens is shown in Figure 21. Similar to the skin damage, the red part represents the damaged element, and the blue part represents the undamaged element.

It can be seen from Figure 21 that the damage of the honeycomb core evolves with the increase of compression load. The honeycomb core of NS00 specimen is first damaged in the chamfering zone, and then the damage zone gradually expands from the chamfering zone to the middle, until the structure is finally damaged. The damage distribution of the PS80 specimen is similar to that of NS00 specimen, but damage appeases around the central lightning damage zone in the compression process, which may be caused by the stress concentration caused by the local depression of the panel in the lightning damage zone. Obviously different from these two specimens, for the NS80 specimen, the honeycomb core is first damaged around the lightning damage on the sides and in the middle. Then, the chamfering zone on the upper end of the honeycomb core is also damaged. With the increase of compression load, the honeycomb core is damaged from the middle to both sides until the structure finally fails.

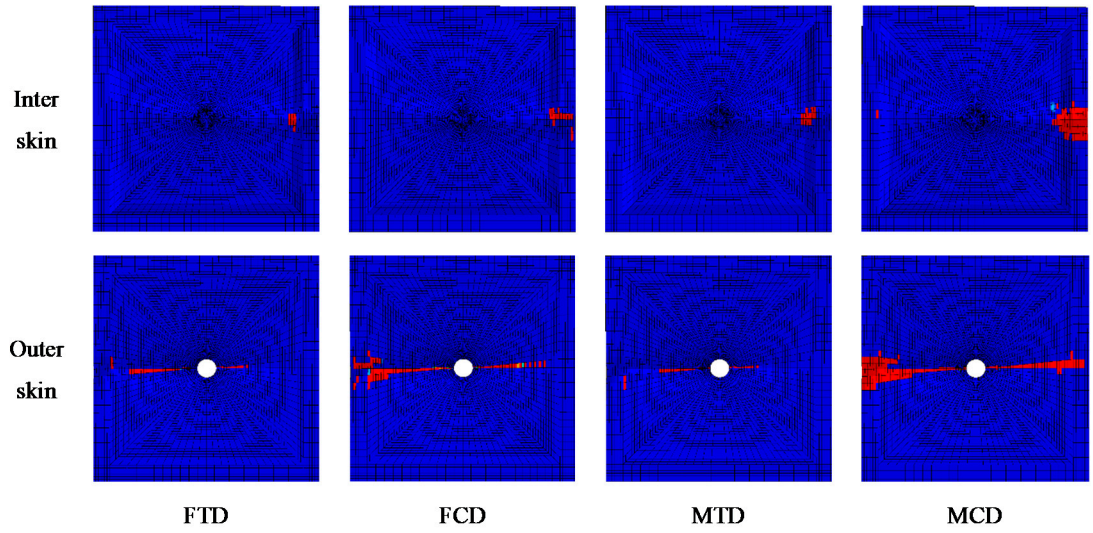


**Figure 20.** Damage distribution of skin in the NS80 specimen.

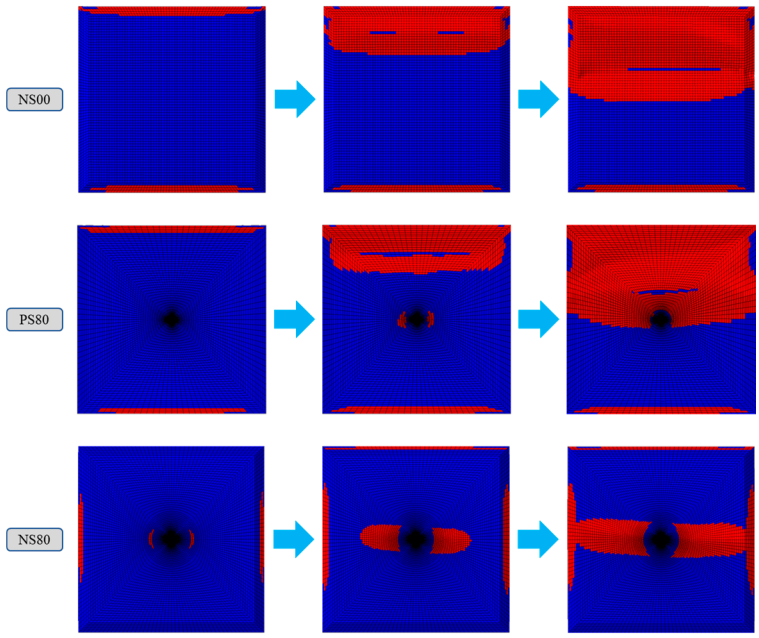


**Figure 21.** The damage distribution and evolution for honeycomb core in specimens.

## 5. Conclusions

In this study, honeycomb sandwich panels with and without a CNTF protection layer were fabricated. Then simulated lightning strike tests were performed on these two types of specimens. Based on this simulated lightning strike test, honeycomb sandwich panel specimens containing different degrees of lightning damage were obtained. Then the residual compressive strength and failure modes of honeycomb sandwich structure after a lightning strike were experimentally studied and analyzed. Finally, the failure modes and damage distribution of the honeycomb sandwich panels after lightning damage were studied by the finite element method. The simulation results were compared with the experimental results, and the following conclusions were drawn:

(1) Lightning strike damage can seriously reduce the bearing capacity of honeycomb sandwich composite structure, while the surface CNTF can reduce lightning damage to a certain extent and improve the residual bearing capacity of composite after lightning strike.

(2) The compression failure modes of honeycomb sandwich panel with closed edge were dependent on the size and extent of the lightning damage. When the lightning damage was small, the compressive failure modes of the specimen were similar to those of the undamaged specimen, and the failure mainly occurred in the chamfering zone of the panel. When the lightning damage was large, the failure of the specimen mainly occurred in the lightning damage zone of the panel.

(3) When lightning was strong enough to completely penetrate the surface skin of the honeycomb sandwich structure, the lightning damage on the skin can be simplified to hole damage with appropriate diameter. Under the proper failure criterion and stiffness degradation rule, the residual strength calculated by progressive damage analysis agrees with the residual strength obtained by testing, which proves the effectiveness of the simulation method to a certain extent.

**Author Contributions:** Methodology, data acquisition, data curation, writing—original draft, Y.W.; methodology, supervision—review and editing, G.Y.; data acquisition, D.Z.; data acquisition, Z.W. All authors have read and agreed to the published version of the manuscript.

**Funding:** This work was supported by the Aeronautical Science Foundation (2017ZA52005) and the Fundamental Research Funds for the Central Universities (NS2021002).

**Institutional Review Board Statement:** Not applicable.

**Informed Consent Statement:** Not applicable.

**Data Availability Statement:** Not applicable.

**Conflicts of Interest:** The authors declare no conflict of interest.

## References

1. Gagné, M.; Therriault, D. Lightning strike protection of composites. *Prog. Aerosp. Sci.* **2014**, *64*, 1–16. [CrossRef]
2. Zhang, X.; Chen, Y.; Hu, J. Recent advances in the development of aerospace materials. *Prog. Aerosp. Sci.* **2018**, *97*, 22–34. [CrossRef]
3. Kumar, V.; Sharma, S.; Pathak, A.; Singh, B.P.; Dhakate, S.R.; Yokozeki, T.; Okada, T.; Ogasawara, T. Interleaved MWCNT buckypaper between CFRP laminates to improve through-thickness electrical conductivity and reducing lightning strike damage. *Compos. Struct.* **2019**, *210*, 581–589. [CrossRef]
4. Katunin, A.; Krukiewicz, K.; Herega, A.; Catalanotti, G. Concept of a conducting composite material for lightning strike protection. *Adv. Mater. Sci.* **2016**, *16*, 32. [CrossRef]
5. Gou, J.; Tang, Y.; Liang, F.; Zhao, Z.; Firsich, D.; Fielding, J. Carbon nanofiber paper for lightning strike protection of composite materials. *Compos. Part B Eng.* **2010**, *41*, 192–198. [CrossRef]
6. Wang, F.; Ji, Y.; Yu, X.; Chen, H.; Yue, Z. Ablation damage assessment of aircraft carbon fiber/epoxy composite and its protection structures suffered from lightning strike. *Compos. Struct.* **2016**, *145*, 226–241. [CrossRef]
7. Hirano, Y.; Katsumata, S.; Iwahori, Y.; Todoroki, A. Artificial lightning testing on graphite/epoxy composite laminate. *Compos. Part A Appl. Sci. Manuf.* **2010**, *41*, 1461–1470. [CrossRef]
8. Feraboli, P.; Kawakami, H. Damage of carbon/epoxy composite plates subjected to mechanical impact and simulated lightning. *J. Aircr.* **2010**, *47*, 999–1012. [CrossRef]
9. Kawakami, H.; Feraboli, P. Lightning strike damage resistance and tolerance of scarf-repaired mesh-protected carbon fiber composites. *Compos. Part A Appl. Sci. Manuf.* **2011**, *42*, 1247–1262. [CrossRef]
10. Kumar, V.; Yokozeki, T.; Okada, T.; Hirano, Y.; Goto, T.; Takahashi, T.; Hassen, A.A.; Ogasawara, T. Polyaniline-based all-polymeric adhesive layer: An effective lightning strike protection technology for high residual mechanical strength of CFRPs. *Compos. Sci. Technol.* **2019**, *172*, 49–57. [CrossRef]
11. Zhang, X.; Zhang, J.; Cheng, X.; Huang, W. Carbon nanotube protected composite laminate subjected to lightning strike: Interlaminar film distribution investigation. *Chin. J. Aeronaut.* **2021**, *34*, 620–628. [CrossRef]
12. Liu, Z.Q.; Yue, Z.F.; Wang, F.S.; Ji, Y.Y. Combining analysis of coupled electrical-thermal and blow-off impulse effects on composite laminate induced by lightning strike. *Appl. Compos. Mater.* **2015**, *22*, 189–207. [CrossRef]
13. Ogasawara, T.; Hirano, Y.; Yoshimura, A. Coupled thermal–electrical analysis for carbon fiber/epoxy composites exposed to simulated lightning current. *Compos. Part A Appl. Sci. Manuf.* **2010**, *41*, 973–981. [CrossRef]
14. Dong, Q.; Guo, Y.; Sun, X.; Jia, Y. Coupled electrical-thermal-pyrolytic analysis of carbon fiber/epoxy composites subjected to lightning strike. *Polymer* **2015**, *56*, 385–394. [CrossRef]
15. Guo, Y.; Xu, Y.; Wang, Q.; Dong, Q.; Yi, X.; Jia, Y. Eliminating lightning strike damage to carbon fiber composite structures in zone 2 of aircraft by Ni-coated carbon fiber nonwoven veils. *Compos. Sci. Technol.* **2019**, *169*, 95–102. [CrossRef]

16. Li, Y.; Li, R.; Lu, L.; Huang, X. Experimental study of damage characteristics of carbon woven fabric/epoxy laminates subjected to lightning strike. *Compos. Part A Appl. Sci. Manuf.* **2015**, *79*, 164–175. [CrossRef]
17. Zhao, Z.; Ma, Y.; Yang, Z.; Yu, J.; Wang, J.; Tong, J.; Yi, X.; Moreira, P.; Sguazzo, C. Light weight non-metallic lightning strike protection film for CFRP. *Mater. Today Commun.* **2020**, *25*, 101502. [CrossRef]
18. Yamashita, S.; Hirano, Y.; Sonehara, T.; Takahashi, J.; Kawabe, K.; Murakami, T. Residual mechanical properties of carbon fibre reinforced thermoplastics with thin-ply prepreg after simulated lightning strike. *Compos. Part A Appl. Sci. Manuf.* **2017**, *101*, 185–194. [CrossRef]
19. Das, S.; Kumar, V.; Lee, J.; Yokozeki, T.; Okada, T. Thickness threshold study of polyaniline-based lightning strike protection coating for carbon/glass fiber reinforced polymer composites. *Compos. Struct.* **2022**, *280*, 114954. [CrossRef]
20. Wang, F.; Ding, N.; Liu, Z.; Ji, Y.; Yue, Z. Ablation damage characteristic and residual strength prediction of carbon fiber/epoxy composite suffered from lightning strike. *Compos. Struct.* **2014**, *117*, 222–233. [CrossRef]
21. Kumar, V.; Yokozeki, T.; Okada, T.; Hirano, Y.; Goto, T.; Takahashi, T.; Ogasawara, T. Effect of through-thickness electrical conductivity of CFRPs on lightning strike damages. *Compos. Part A Appl. Sci. Manuf.* **2018**, *114*, 429–438. [CrossRef]
22. Zhao, Z.; Xian, G.; Yu, J.; Wang, J.; Tong, J.; Wei, J.; Wang, C.; Moreira, P.; Yi, X. Development of electrically conductive structural BMI based CFRPs for lightning strike protection. *Compos. Sci. Technol.* **2018**, *167*, 555–562. [CrossRef]
23. Wang, F.; Yu, X.; Jia, S.; Li, P. Experimental and numerical study on residual strength of aircraft carbon/epoxy composite after lightning strike. *Aerosp. Sci. Technol.* **2018**, *75*, 304–314. [CrossRef]
24. Rajesh, P.; Sirois, F.; Therriault, D. Damage response of composites coated with conducting materials subjected to emulated lightning strikes. *Mater. Des.* **2018**, *139*, 45–55. [CrossRef]
25. Dhanya, T.; Yerramalli, C.S. Lightning strike effect on carbon fiber reinforced composites–effect of copper mesh protection. *Mater. Today Commun.* **2018**, *16*, 124–134. [CrossRef]
26. Guo, Y.; Xu, Y.; Zhang, L.; Wei, X.; Dong, Q.; Yi, X.; Jia, Y. Implementation of fiberglass in carbon fiber composites as an isolation layer that enhances lightning strike protection. *Compos. Sci. Technol.* **2019**, *174*, 117–124. [CrossRef]
27. Kumar, V.; Yokozeki, T.; Karch, C.; Hassen, A.A.; Hershey, C.J.; Kim, S.; Lindahl, J.M.; Barnes, A.; Bandari, Y.K.; Kunc, V. Factors affecting direct lightning strike damage to fiber reinforced composites: A review. *Compos. Part B Eng.* **2020**, *183*, 107688. [CrossRef]
28. Xia, Q.; Mei, H.; Zhang, Z.; Liu, Y.; Liu, Y.; Leng, J. Fabrication of the silver modified carbon nanotube film/carbon fiber reinforced polymer composite for the lightning strike protection application. *Compos. Part B Eng.* **2020**, *180*, 107563. [CrossRef]
29. Han, J.-H.; Zhang, H.; Chen, M.-J.; Wang, D.; Liu, Q.; Wu, Q.-L.; Zhang, Z. The combination of carbon nanotube buckypaper and insulating adhesive for lightning strike protection of the carbon fiber/epoxy laminates. *Carbon* **2015**, *94*, 101–113. [CrossRef]
30. Herrmann, A.S.; Zahlen, P.C.; Zuardy, I. *Sandwich Structures Technology in Commercial Aviation*; Springer: Dordrecht, The Netherlands, 2005.
31. Jérôme, P. Composite Materials in the Airbus A380. From History to Future. In Proceedings of the 13th International Conference on Composite Materials (ICCM-13), Beijing, China, 25–29 June 2001; Volume 1, pp. 25–29.
32. *SAE ARP-5416*; Aircraft Lightning Test Methods. SAE Aerospace Group: Washington, DC, USA, 2005.
33. Pan, S. Research on Damage and Scarf Repair of Edge Closed Honeycomb Sandwich Panels. Master's Thesis, Nanjing University of Aeronautics and Astronautics, Nanjing, China, 2019.
34. Hashin, Z. Failure criteria for unidirectional fiber composites. *J. Appl. Mech.* **1980**, *47*, 329–334. [CrossRef]
35. Zhang, F.; Mohmmed, R.; Sun, B.; Gu, B. Damage behaviors of foam sandwiched composite materials under quasi-static three-point bending. *Appl. Compos. Mater.* **2013**, *20*, 1231–1246. [CrossRef]
36. Yuan, J.; Zhang, L.; Huo, Z. An equivalent modeling method for honeycomb sandwich structure based on orthogonal anisotropic solid element. *Int. J. Aeronaut. Space Sci.* **2020**, *21*, 957–969. [CrossRef]
37. Hu, N.; Wang, W.; Leng, G. Study on equivalent modeling of honeycomb sandwich panels for large radio telescopes. *Lect. Notes Inf. Technol.* **2012**, *15*, 2012.
38. Besant, T.; Davies, G.; Hitchings, D. Finite element modelling of low velocity impact of composite sandwich panels. *Compos. Part A Appl. Sci. Manuf.* **2001**, *32*, 1189–1196. [CrossRef]
39. Fan, X.L.; Wang, T.J.; Sun, Q. Damage evolution of sandwich composite structure using a progressive failure analysis methodology. In Proceedings of the 11th International Conference on the Mechanical Behavior of Materials (ICM11), Como, Italy, 5–9 June 2011.
40. Camanho, P.P.; Davila, C.G.; De Moura, M. Numerical simulation of mixed-mode progressive delamination in composite materials. *J. Compos. Mater.* **2003**, *37*, 1415–1438. [CrossRef]
41. Benzeggagh, M.L.; Kenane, M. Measurement of mixed-mode delamination fracture toughness of unidirectional glass/epoxy composites with mixed-mode bending apparatus. *Compos. Sci. Technol.* **1996**, *56*, 439–449. [CrossRef]
42. Tafreshi, A.; Oswald, T. Global buckling behaviour and local damage propagation in composite plates with embedded delaminations. *Int. J. Press. Vessel. Pip.* **2003**, *80*, 9–20. [CrossRef]